

# Sunlight penetration dominates the thermal regime and energetics of a shallow ice-covered lake in arid climate

Wenfeng Huang<sup>1,2\*</sup>, Wen Zhao<sup>1</sup>, Cheng Zhang<sup>1</sup>, Matti Leppäranta<sup>3</sup>, Zhijun Li<sup>4\*</sup>, Rui Li<sup>1</sup>, Zhanjun Lin<sup>2</sup>

1 Key Laboratory of Subsurface Hydrology and Ecological Effects in Arid Region (the Ministry of Education), Chang'an University, Xi'an, China

2 State Key Laboratory of Frozen Soil Engineering, Northwest Institute of Eco-Environment and Resources, Chinese Academy of Science, Lanzhou, China

3 Institute of Atmospheric and Earth Sciences, University of Helsinki, Helsinki, Finland.

4 State Key Laboratory of Coastal and Offshore Engineering, Dalian University of Technology, Dalian, China

\*Correspondence to: Wenfeng Huang ([huangwenfeng@chd.edu.cn](mailto:huangwenfeng@chd.edu.cn)) and Zhijun Li ([lizhijun@dlut.edu.cn](mailto:lizhijun@dlut.edu.cn))

**Abstract.** The Mongolian Plateau is characterized by cold and arid winter with very little precipitation (snowfall), strong solar insolation, and dry air. But little is known about the thermal regimes of ice and ice-covered lakes and their response to the distinct weather and climate in this region. In a typical large, shallow lake, ice/snow processes(cover) and under-ice thermodynamics were monitored for four winters in 2015–2019. Heat transfer at the ice–water interface and lake heat budget were investigated. The results revealed that persistent bare ice of 35–50 cm permits 20–35% of incident solar radiation to get transmitted into the under-ice water, providing the source for under-ice energy flows and causing/maintaining high water temperature (up to 6–8°C) and high heat flux from water to ice (averages of 20–45 W m<sup>-2</sup>) in mid-winter along with higher heat conduction in the ice interior during freezing. The heat balance shows that the transmitted radiation and the heat flux from water to ice are the dominant and highly correlated heat flows in the lake. Both bulk water temperature and temperature structure are sensitive to solar transmittance and occasional snow events. Under-ice convective mixing does not necessarily occur because of stratification of salinity in the water body. Especially, salt exclusion in freezing changes both the bulk salinity and the salinity profile that plays a major role in the stability and mixing of the water column in this shallow lake.

## 1 Introduction

Lakes are important water resources and provide vital habitats for aquatic ecosystems. More than 55% of world lakes are located between 40 and 80°N in the northern hemisphere (Verpoorter et al., 2014) and have potential to freeze seasonally (Kirillin et al., 2012), especially in Arctic, boreal, and temperate climate, and high mountain regions. Due to distinct properties of ice compared to water, seasonal formation and decay of ice cover have tremendous impacts on the lake water quality (Yang et al., 2016), physical and chemical conditions (Yang et al., 2021; Cavaliere and Baulch, 2018; Huang et al., 2019a), aquatic ecosystem (Griffiths et al., 2017; Song et al., 2019), and land-atmosphere mass and heat interaction (Wang et al., 2015; Franz et al., 2018). Therefore, common concerns have been widely

39 spread on mapping lake ice physics and its underlying physical mechanisms in the evolution of ice  
40 seasons.

41 Field and modeling investigations on lake ice processes have a long history in northern temperate and  
42 boreal regions, such as Fennoscandia, central Europe, northern Canada, and the Great Lakes.  
43 Shortening of ice cover period has been documented currently in lakes in these northern regions  
44 (Bernhardt et al., 2012; Lei et al., 2012; Karetnikov et al., 2017; Ptak et al., 2020). However, the lake  
45 ice regime has remained less studied due to lack of long-term observational records in arid climate  
46 regions, such as central Asia and high mountains, which are subject to a quite different landscape,  
47 regional climate, and hydrological cycles compared with the northern temperate, boreal, and Arctic  
48 environment.

49 Lake thermal stratification is of great importance to hydrodynamics and transport of nutrients, oxygen,  
50 and primary production, which influence limnological habitats and ecosystems. In freezing freshwater  
51 lakes, stable inverse thermal stratification usually forms and persists under the ice cover with the  
52 temperature smaller than the maximum density temperature ( $3.98^{\circ}\text{C}$ ). After the onset of melting, strong  
53 solar irradiance can penetrate the ice cover into the water and drive turbulent convection (Bouffard et  
54 al., 2019; Volkov et al., 2019) until the bulk temperature reaches or surpasses the maximum density  
55 temperature or until breakup (Yang et al., 2020). However, in some shallow mid-latitude brackish lakes,  
56 this is not the story. During melting period, a warm middle layer may form due to salinity stratification  
57 and separate the overlying inverse thermal stratification and the underlying positive thermal  
58 stratification. The temperature of this warm layer can go up to around  $10^{\circ}\text{C}$  before the breakup (e.g.  
59 Huang et al., 2019b; Kirillin et al., 2021). This underlines the uniqueness of seasonally ice-covered  
60 lakes in mid-latitude arid regions and the importance of their different climate. It still remains unclear  
61 how this stratification forms and evolves and how it interacts with the snow/ice cover.

62 After freeze-up, the ice cover shelters the lake from atmospheric forcing and deposits. The lake  
63 boundary constitutes of only the ice cover on the top and sediment at the bottom. The heat budget is  
64 governed by radiative and sensible fluxes across the ice-water-sediment interfaces (Leppäranta, et al.,  
65 2019). But these fluxes, including solar radiation transfer, ice-water heat exchange, and sediment heat  
66 release, have not been well quantified in mid-latitude arid region lakes. Especially, the ice-water heat  
67 flux, a key factor affecting the mass and energy balance of both ice and water, has been demonstrated  
68 to be remarkably higher in Central Asia than in Arctic and boreal zones (Malm et al., 1997; Jakkila et  
69 al., 2009; Huang et al., 2019a,b; Lu et al., 2020). But the regime underpinning its high values is still  
70 unknown.

71 To fill the knowledge gaps in winter thermodynamics of lakes in cold and arid Asia and their  
72 background energy flows, we performed a four-winter observation program of snow/ice processes,  
73 solar radiation transfer, and temperature profiles of air-ice-water-sediment column in a typical large  
74 shallow lake that is seasonally ice-covered for 4–5 months, located in the southern border of the  
75 Mongolia Plateau. Below, observations and models are combined 1) to reveal the seasonal and diurnal  
76 dynamics of the temperature stratification under ice in the mid-latitude arid climate, and 2) to quantify  
77 and balance the involved heat fluxes that determine the thermal state of the lake.

## 78 **2 Data and methods**

### 79 **2.1 Study site**

80 The Hetao Basin (ca.  $6,000\text{ km}^2$ , mean altitude  $> 1,000\text{ m}$ ), one of the oldest and largest irrigation areas  
81 in China, is located in the central southern Mongolian Plateau controlled by temperate continental

82 climate. In the Hetao Basin, the annual sunshine duration is 3,000–3,200 h, the annual air temperature  
83 is 5.6–7.4°C with the lowest and highest **monthly** temperature of –14– –11°C (Jan) and 22–24°C (Jul),  
84 the frost-free period is 130–150 d, and the annual precipitation is 150–400 mm concentrated **in the**  
85 **warm season**. Most parts of the basin have been desertified or semi-desertified in recent decades.  
86 Lake Ulansuhai (40°36′–41°03′N, 108°41′–108°57′E, altitude 1,019 m) is a typical large, shallow lake  
87 in desert/semi-desert region with a total area of about 306 km<sup>2</sup> (Fig. 1). It is a very important part of the  
88 irrigation and drainage system of the Hetao Basin, and its major water source comes from the farmland  
89 irrigation drainage and domestic sewage. The maximum and mean depths are 2.5–3.0 m and 1.0–1.5 m,  
90 respectively. The annual air temperature, hours of sunshine, precipitation, evaporation, wind speed,  
91 frost-free period are 7.3°C, 3,185 h, 224 mm, 1,502 mm, 3.5 m s<sup>-1</sup>, and 152 d, respectively (Sun et al.,  
92 2011). The solar noon-time and altitude in winter are 12:45±15 min and 41±10°, respectively. The ice  
93 cover is usually free of snow or only sparsely snow-covered due to occasional **snowfall** events and  
94 strong winds.

95 The lake **surface elevation** is regulated through pumping water from the Yellow River via the main  
96 inflow canal at the western **shore**. The total annual water supply is approximately  $4 \times 10^8$  m<sup>3</sup>,  
97 equivalent to the lake volume. But in winter (Nov–Mar), very little surface inflow/outflow exists  
98 except possible **minor** wastewater inflow (Sun et al., 2013), and the subsurface inflow is also negligible  
99 (Zhu et al., 2014). For more detailed information, please **consult** Lu et al. (2020) and references therein.

100 According to our sampling tests in winter 2017, the lake water is **brackish or** weakly saline with  
101 salinity of 1.0–1.5 PSU before the ice-on and gradually **increasing** to 2.5–3.0 PSU **due to exclusion of**  
102 **salts** when the ice grows to its annual maximum.

103 **Due to its unique climate and eutrophication, the lake ecology under the ice cover is very active with**  
104 **high rates of primary production and respiration. This is believed to be highly related to the under-ice**  
105 **solar irradiance and temperature and the key role of ice and snow processes (Song et al., 2019; Huang**  
106 **et al., 2021). Our previous observations revealed the mass and heat balance of the lake ice cover and**  
107 **the impacts of warm water under the ice cover (Lu et al., 2020), but further investigations were**  
108 **performed and combined here to look into the thermal stratification regimes.**

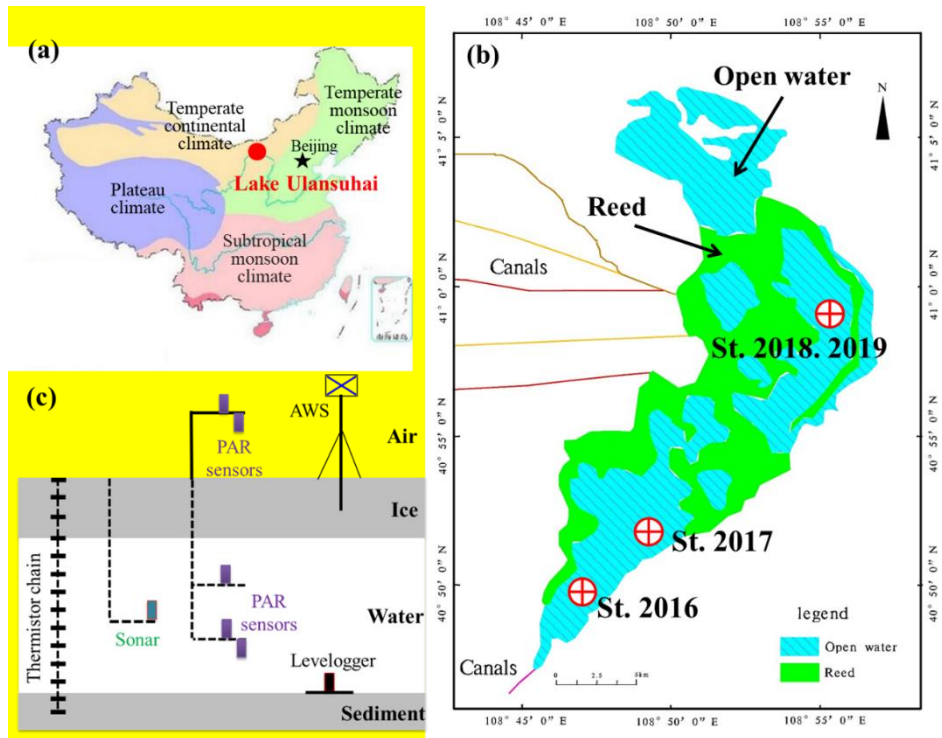
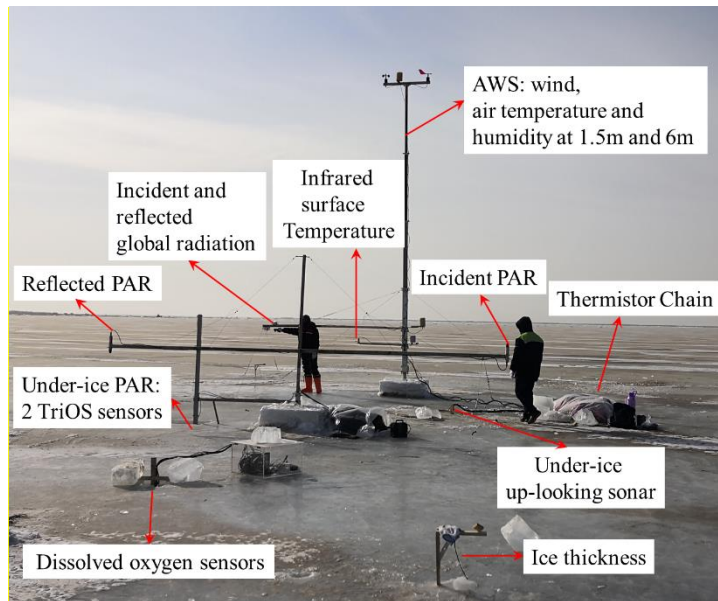


**Figure 1. Locations of Lake Ulansuhai (a) and study sites (b) and the field instrumentation (c). In each winter, a thermistor chain was refrozen into ice cover to measure temperature profile of the air-ice-water-sediment column with an established automatic weather station (AWS); more than 3 radiation sensors over photosynthesis active radiation (PAR) band were deployed to observe the incident, reflected and transmitted solar radiation.**

## 2.2 Data acquisition

During winters of 2015-2019, field campaigns were conducted in open, reed-free areas of Lake Ulansuhai (Figs. 1c and 2). In each winter, an automatic weather station (AWS) was established on the ice cover, to record wind speed and direction, air temperature and humidity, incident and reflected global radiation (300–3000 nm), and the skin temperature of the ice/snow surface. An under-ice uplooking sonar (WUUL-1/2, Wuhan University, China) was used to measure the ice thickness evolution with the accuracy of 2 mm. Snow thickness was measured manually using a snow stake every 1–2 days. The temperature profile of the air-ice-water-sediment column was observed using a thermistor chain (PTWD, Jinzhou Sunshine Technology Co. Ltd, China) at 5–10 cm spacing with the accuracy of 0.05°C. TriOS spectral radiometers with the accuracy of 0.04–0.06 mW m<sup>-2</sup> nm<sup>-1</sup> (RAMSES-ACC-VIS, TriOS, German) were used to measure the incident and reflected photosynthetically active radiation (PAR) over the ice/snow surface and under the ice cover. The water level was monitored using a temperature-pressure logger with an accuracy of 0.05% (LTC Levellogger, Solinst, Canada) placed 20 cm above the sediment surface. All the above variables were recorded every 10 min. Information of the acquired datasets is summarized in Table 1 (see also Huang et al. 2021).

In the winter of 2017, the under-ice water electric conductivity (EC) was measured using 3 online conductivity loggers (HOBO U24, Onset, USA) at depths of 60 cm, 100 cm, and 150 cm from Jan 21 to Mar 11 (Table 1). Concurrently, ice and water samples with 5 cm spacing were collected 8 times this winter to measure their EC and salinity using a portable YSI salinometer.



135

136 **Figure 2. Field setup of apparatus deployed and corresponding monitored variables in winter of**  
 137 **2019**

138

**Table 1. Data series acquired during the four-winter observation program**

Winter	2016	2017	2018	2019
Available duration	Jan 11–Mar 9	Jan 21–Mar 11	Jan 9–Feb 25	Jan 20–Feb 27
Water depth	220 cm	170 cm	143 cm	140 cm
Ice/snow thickness	√	√	√	√
Air-ice-water-sediment temperature	5 cm spacing in ice, 10–15 cm spacing in water and sediment	5 cm spacing in ice, 5–10 cm spacing in water and sediment	5 cm spacing in ice, 5–10 cm spacing in water and sediment	5 cm spacing in ice, 10 cm spacing in water and sediment
Under-ice irradiation	175 cm	80 cm, 130 cm	65 cm, 90 cm, 120 cm	80 cm, 120 cm
Under-ice upwelling radiation		105 cm	100 cm	
Water level		√		
Electric Conductivity		60 cm, 100 cm, 150 cm		

139

**Note: the observed depths for under-ice irradiation and upwelling radiation and electric conductivity denote the distances below the ice surface.**

140

141

### **2.3 Heat flux calculation and balance**

142

In freshwater lakes, the water temperature is colder than 3.98°C with a weak inverse thermal stratification during freezing (Winter I stage), and typically a convective mixing layer forms between the top cold interfacial layer and the warm quiescent layer during melting (Winter II stage) (Kirillin et al., 2012). The stratification structure in Lake Ulansuhai was checked using temperature gradient following Kirillin et al. (2018).

147

After freeze-up, as illustrated in Fig. 3, the thermal regime of the water column is governed by the solar irradiance penetrating through the ice cover ( $R_w$ ), solar radiation absorbed by the lake sediment (if any)

148

149 ( $R_{sed}$ ), heat fluxes through ice-water ( $F_w$ ) and water-sediment ( $F_{sed}$ ) interfaces, and horizontal heat gain  
 150 by advection and diffusion ( $F_h$ ) from the neighboring water body. If the zero-reference level for heat is  
 151 defined as the heat content of liquid fresh water at its freezing point temperature, the heat content of  
 152 water is  $\rho_w c_w T_w h_w$ , and the heat budget of a water column is

$$153 \quad R_w - R_{sed} + F_{sed} + F_h - F_w = \rho_w c_w h_w \frac{dT_w}{dt} + \rho_w c_w T_w \frac{dh_w}{dt}, \quad (1)$$

154 where  $\rho_w$ ,  $c_w$ , and  $T_w$  are the density, specific heat, and bulk temperature of water, respectively. Other  
 155 variables are defined in Fig. 3. The lateral heat transport  $F_h$  is negligible in this shallow lake with a flat  
 156 bottom (Rizk et al., 2014; Kirillin et al., 2015). The two terms on the right-hand side are the heat  
 157 content changes induced by changes in the water temperature and depth, respectively. The water level  
 158 logger indicated that the lake lost water through seepage to soil quite slowly (about 0.6 mm/d) during  
 159 ice seasons, and the heat loss due to the bottom water seepage was estimated to be smaller than 0.8 W  
 160 m<sup>-2</sup> and thus was ignored as a minor term compared to the other heat fluxes.

161 *Under-ice solar irradiance.* The light extinction coefficient of the under-ice water was measured as 2.1  
 162 m<sup>-1</sup> under a clear sky on Jan 7, 2018. Using the observed irradiance by under-ice spectral sensors, the  
 163 solar irradiance at the ice-water interface ( $R_w$ ) was derived from a one-band exponential decay law of  
 164 light transfer in water column, following

$$165 \quad R_w = R_d \exp(\kappa_w(z_d - h_i)), \quad (2)$$

166 where  $R_d$  is the observed downward irradiance at depth  $z_d$ ,  $h_i$  is the ice thickness, and  $\kappa_w$  is the light  
 167 extinction coefficient of water.

168 *Sediment heat flux.* The heat exchange flux through the water-sediment interface ( $F_{sed}$ ) was calculated  
 169 with the gradient method,

$$170 \quad F_{sed} = -\kappa_{sed} \left. \frac{\partial T_{sed}}{\partial z} \right|_{bottom} \approx -\kappa_{sed} \frac{\Delta T_{sed}}{\Delta z}, \quad (3)$$

171 where  $\kappa_{sed}$  is the thermal conductivity of sediment and  $T_{sed}$  is the observed sediment temperature. In the  
 172 winter of 2018, four thermistors were buried in the sediment (1 cm, 9cm, 17 cm, and 30 cm below the  
 173 sediment surface) to measure the sediment temperature profiles. Assuming the heat transfer in the top  
 174 sediment is governed by the typical one-dimensional vertical heat conduction equation, an optimal  
 175 control model was deployed to retrieve the effective thermal diffusivity of the sediment was estimated  
 176 based on the observed sediment temperature profiles. For details on the optimal control model, please  
 177 refer to Shi et al. (2014). The thermal conductivity can be determined (0.2–0.7 W m<sup>-1</sup>°C<sup>-1</sup>) with  
 178 measured density and specific heat capacity of sediment.  $\kappa_{sed} = 0.5$  W m<sup>-1</sup>°C<sup>-1</sup> was used in Eq. 2.

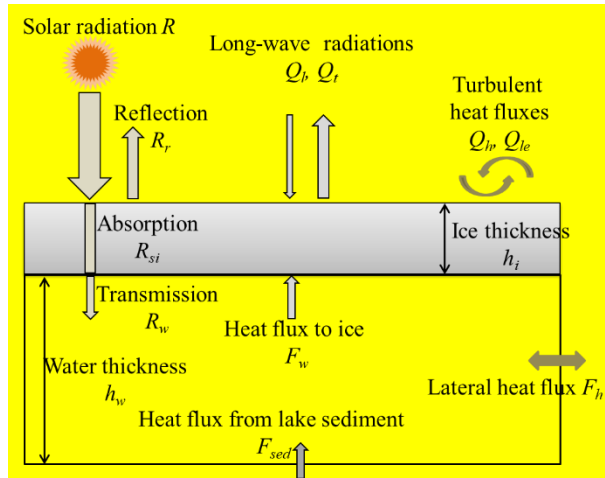
179 *Water-to-ice heat flux.* The water-to-ice heat flux can be derived from the heat balance at the ice-water  
 180 interface,

$$181 \quad F_w = Q_c - Q_l = -\kappa_i \left. \frac{\partial T_i}{\partial z} \right|_{z=h_i} - \rho_i L_f \frac{\partial h_i}{\partial t}, \quad (4)$$

182 where  $Q_c$  and  $Q_l$  are the conductive heat flux to ice and the latent heat due to freezing/melting,  
 183 respectively, and  $\rho_i$  and  $L_f$  are the density and latent heat of fusion of ice, respectively. The first term  
 184 denotes the heat conduction into the ice interior, which can be derived using the temperature gradient in  
 185 the bottom ice layer. The second term on the right-hand side denotes the heat release/absorption due to  
 186 freezing/melting, which can be derived from ice thickness observations.



187 The heat content due to temperature change (i.e., the first term on the right-hand side of Eq. 1) was  
 188 calculated using the observed water temperature profiles.  
 189 Direct use of semi-hourly observed datasets brought high-frequency fluctuations in estimated heat flux,  
 190 and then daily means were used for further analysis on seasonal dynamics.



191  
 192 **Figure 3. Heat budget components of the water column under the ice (modified from Huang et al,**  
 193 **2019b).**

194  
 195 **2.4 Potential errors in heat flux estimation**

196 Potential errors in the above heat flux estimation usually come from the measurement accuracy of the  
 197 deployed apparatuses. The maximum error for each flux was determined based on the related apparatus  
 198 accuracy (Table 2). The thermistor accuracy is expected to lead to errors less than  $1.7 \text{ W m}^{-2}$  on  $F_s$  and  
 199  $F_{T_w}$ , and the ice density caused errors less than  $1.3 \text{ W m}^{-2}$  on  $F_w$ . Other heat fluxes suffer to only  
 200 negligible uncertainties ( $< 0.3 \text{ W m}^{-2}$ ) induced by individual sources. Errors from several sources may  
 201 accumulate especially in  $F_w$ , but the accumulated errors in  $F_w$  should be less than 8%.

202  
 203 **Table 2. Uncertainties in calculation of heat fluxes**

Error source	Errors in heat flux ( $\text{W m}^{-2}$ )*			
	$R_w$	$F_{sed}$	$F_w$	$F_{T_w} = \rho_w c_w h_w \frac{dT_w}{dt}$
Radiation precision	0.08	-	-	-
Thermistor precision	-	0.25	1.1	1.7
Ice thickness	0.1	-	-	0.01
Ice growth rate	-	-	0.3	-
Ice density	-	-	1.25	-
Water density	-	-	-	0.2

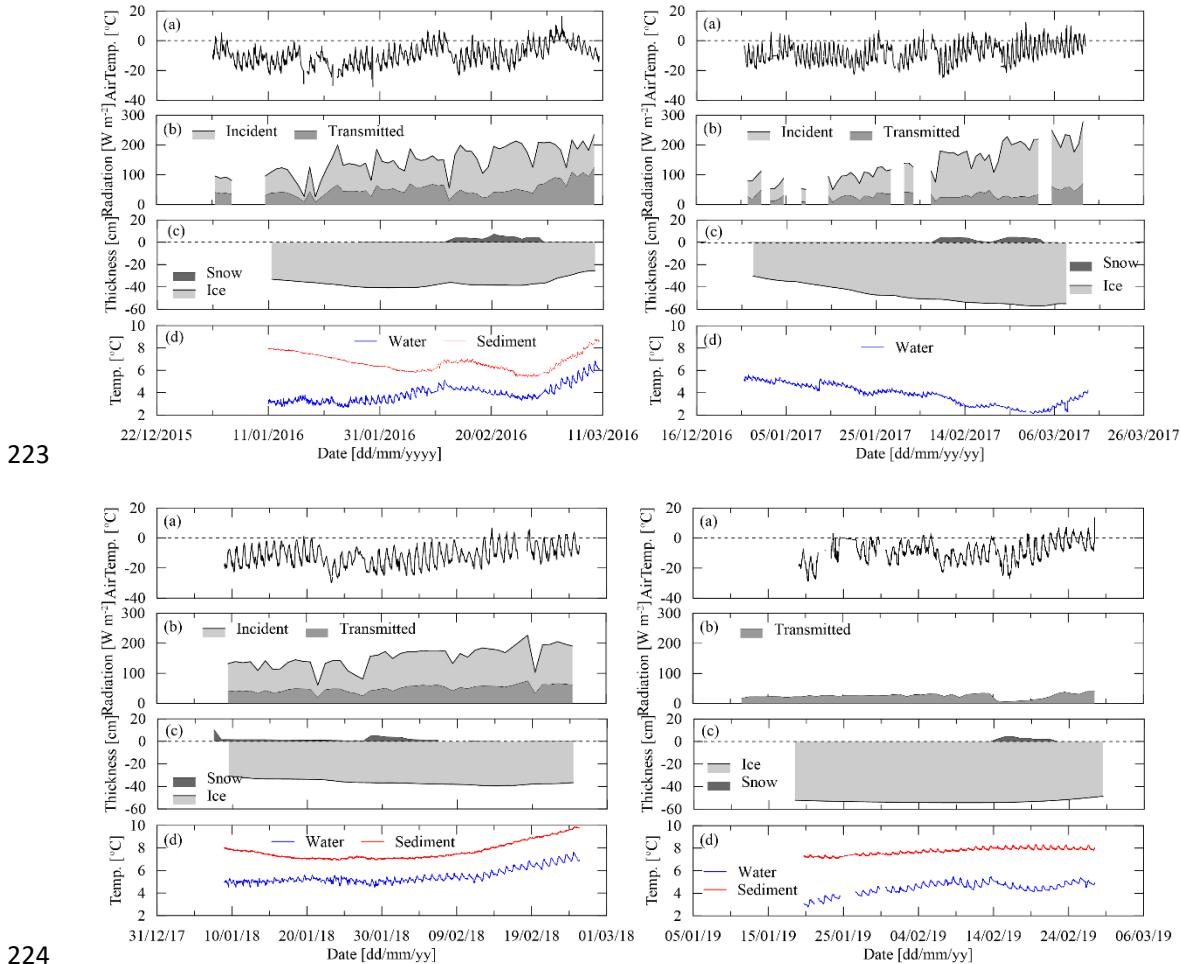
204 \* Dashes (-) indicate inapplicable.

205 **3 Results**

206 **3.1 Lake ice and temperature**

207 Our observations were conducted during mid-winter covering the turning point from ice growth to  
 208 melting. The air temperature was consistently lower than  $0^\circ\text{C}$ , but its daily amplitude was very high

209 (10–16°C) and the peak at noon/afternoon could be close to 0°C (Fig. 4). Wind speed was generally  
 210 lower than 4 m s<sup>-1</sup> except occasional gusts that led to snow or dust drifting. The relative humidity of air  
 211 2-m above the ice surface also showed an evident diurnal cycle between 40% and 80%.  
 212 The peak incident solar radiation was each day roughly 500–800 W m<sup>-2</sup>, and its daily average was 80–  
 213 200 W m<sup>-2</sup> showing an increasing trend from the beginning to the end of our observation period. But  
 214 the daily average was always smaller than 100 W m<sup>-2</sup> due to prevailing cloudy or overcast skies in  
 215 winter 2019. Occasional snowfalls usually brought thin snow layers (< 6 cm) that continuously ablated  
 216 due to wind blowing and melting and sublimation. A new snow cover could increase the surface albedo  
 217 up to over 0.80 but this increment gradually disappeared within one week following the snowfall.  
 218 The maximum annual ice thickness varied between 35 cm and 60 cm, accounting for 30%–60% of the  
 219 mean lake depth. The bulk water temperature under ice cover was 3–7°C and showed diurnal cycles  
 220 and synoptic decreases following snowfall events, evidencing the decrease of transmitted solar  
 221 radiation. The sediment surface layer was always warmer than the water column during the observation  
 222 period, showing that the sediment works as a heat source to the overlying water.



225 **Figure 4.** Observational air temperature  $T_a$  (a), daily means of incident and transmitted solar  
 226 radiation (b), snow and ice thickness (c), temperature of water column and surface sediment. (top  
 227 left: winter 2016; top right: winter 2017; bottom left: winter 2018; bottom right: winter 2019)

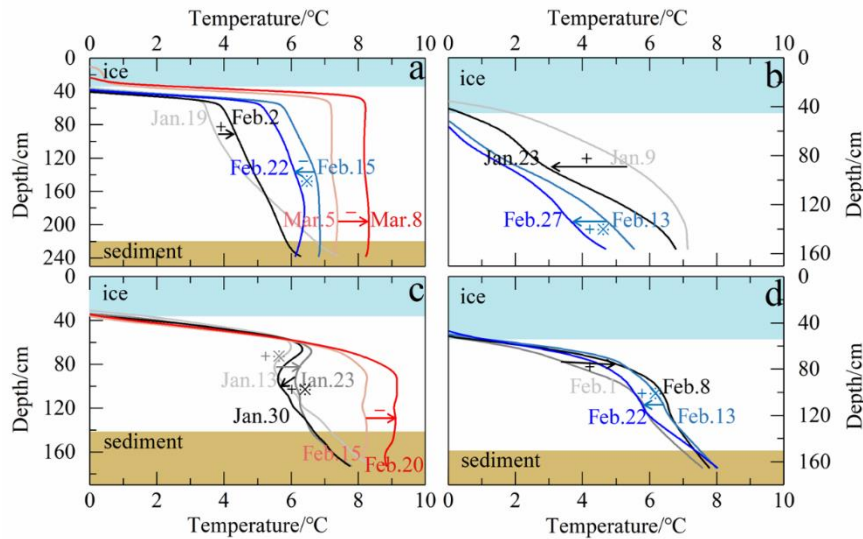
228  
 229 **3.2 Thermal stratification and mixing in midwinter**



230 In mid-winter, the lake sediment was still very warm with surface temperature  $> 6^{\circ}\text{C}$ , usually causing  
231 temperatures higher than  $4^{\circ}\text{C}$  in the lower part of water column (Fig. 5). It is hypothesized that this  
232 stratification was supported by salinity stratification. There is no detailed concurrent salinity profile  
233 data available, but the bulk salinity is of the order of 1 PSU, enriched in ice season. As was observed in  
234 the winter of 2017 (Fig. 6), stable salinity stratification existed during the freezing period, and as salt  
235 was continuously excluded to water through the ice-water interface during water freezing, the bulk  
236 salinity increased and the salinity structure approached gradually to neutral stratification. But when the  
237 ice melting began on Mar 7, the bulk salinity decreased and stable salinity stratification formed again  
238 due to fresher meltwater intrusion. The sensitivity of density to temperature is very low in the  
239 neighborhood of  $4^{\circ}\text{C}$  so that quite small salinity changes can compensate for the observed temperature  
240 structure for neutral density stratification. Although our observations didn't cover the whole ice season,  
241 evident seasonal and annual variations were observed.

242 A common thin layer (10–30 cm) of strong inverse stratification (i.e., interface layer) prevailed just  
243 beneath the ice due to the large difference in temperature of the ice base at the freezing point and the  
244 bulk water column, e.g. in winters 2016, 2018 and 2019. But in winter 2017, this thin top layer did not  
245 show up and a persistent thick inverse structure developed through the water column (Fig. 5b).  
246 Underneath the top cold interface layer, the temperature increased slowly downward to the warm  
247 sediment (weak inverse structure) in winter 2019 and prior to 3 Mar in winter 2016 (Fig. 5a and 5d).  
248 After 3 Mar in winter 2016 and 10 Feb in winter 2018, a thermally homogeneous convective layer  
249 quickly developed after the bulk water temperature rose above approximately  $7^{\circ}\text{C}$  (Fig. 5a and 5c).  
250 Strikingly, before the formation of convective mixing in winter 2018, a “warm” zone of 30 cm (local  
251 maximum temperature) with temperature decreasing both downwardly and upwardly persisted at  $\sim 30$   
252 cm beneath the ice base. This abnormal layer is sometimes called a local temperature minimum  
253 (Mironov et al., 2002) or a “temperature dichotomy” (i.e., a dicothermal layer used in oceanography)  
254 (e.g., Kirillin et al., 2011, 2021). Water temperature contours (not shown) revealed that both the bulk  
255 temperature and thickness of the dicothermal layer show significant diurnal cycles: its temperature and  
256 thickness take up and increase following the solar insolation cycle and decrease or even disappear  
257 during the night. The development and extension of this layer also increase the thermal gradient of the  
258 overlying interface layer.

259 Occasional snowfall events usually led to quick bulk cooling along the entire water temperature profile  
260 due to the high reflection of new snow despite their small thickness. The sensitive response of water  
261 temperature to snow events (actually changes in penetrated radiation) implies large heat flux from  
262 water to ice and the dominance of solar radiation in this lake.



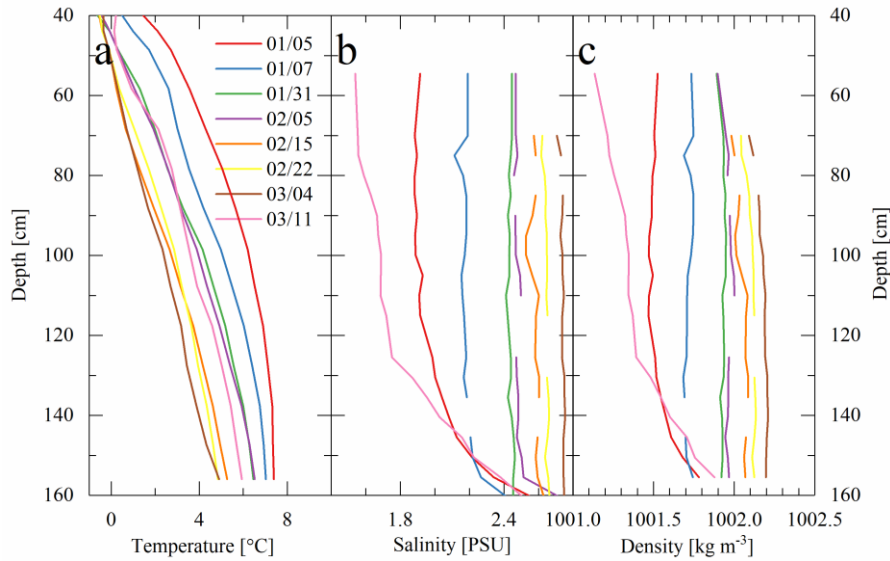
263

264 **Figure 5. Daily profile evolution of water column during ice season of winters (a) 2016, (b) 2017,**  
 265 **(c) 2018, and (d) 2019. Light blue and brown zones denote ice cover and bottom sediment,**  
 266 **respectively. Asterisks (×) denote snowfalls and snow-covered periods. Plus (+) and minus (-)**  
 267 **denote the growth and melt stage of the ice cover.**

268

269 Unconventionally, under-ice convection did not take place in all winters (only two of our four  
 270 observational winters) and seems to develop just when the bulk water temperature goes up to 7°C. This  
 271 temperature threshold is higher than the temperature of maximum density of freshwater (3.98°C) and  
 272 saline water (<3.98°C). These annually variable convections are believed to form conditionally and  
 273 lake-specifically with proper water-sediment temperature and salinity profile. **When the water**  
 274 **temperature is large enough, its density effect overcomes salinity stratification and convection is thus**  
 275 **triggered.** Taking winter of 2017 as an example, water sampling indicated that, in this very shallow lake,  
 276 **the salinity increased and its profile structure changed simultaneously as the ice grew (Fig. 6).** At the  
 277 ice-on, the salinity showed a stable profile (increasing downwardly) and its impact on water density  
 278 outweighed the impact of concurrent temperature gradient (i.e., on Jan 5). With the following ice  
 279 growth, the bulk salinity increased but the salinity gradient decreased, and the temperature gradient  
 280 decreased. Consequently, the weakened salinity gradient could persistently outweigh or offset the  
 281 impact of temperature profile on water density through the growing period (before Mar 4). **Otherwise,**  
 282 **if the weakening gradient of salinity no longer offsets the temperature effect, the convective mixing**  
 283 **takes place across the density instability layer. This is very likely why under-ice mixing occurred in the**  
 284 **winters of 2016 and 2018.** When the ice started melting, the salinity gradient turned larger due to fresh  
 285 meltwater released from the top, **the water column or the top layer became more stable (on Mar 11).**

286 We can conclude that how the water temperature and salinity profiles change synchronously during late  
 287 freezing and initial melting determines whether the under-ice convection takes place. Especially, if the  
 288 sediment temperature is high and the transmitted radiation is large during freezing, the sediment and  
 289 bottom water temperature can be warm and increase rapidly, increasing the probability for full-depth  
 290 convection such as in the winters of 2016 and 2018.



291

292 **Figure 6. Observed temperature and salinity profiles and estimated water density (according to**  
 293 **Leppäranta (2015)) in winter 2017.**

294

### 295 3.3 Heat transfer at the ice-water interface

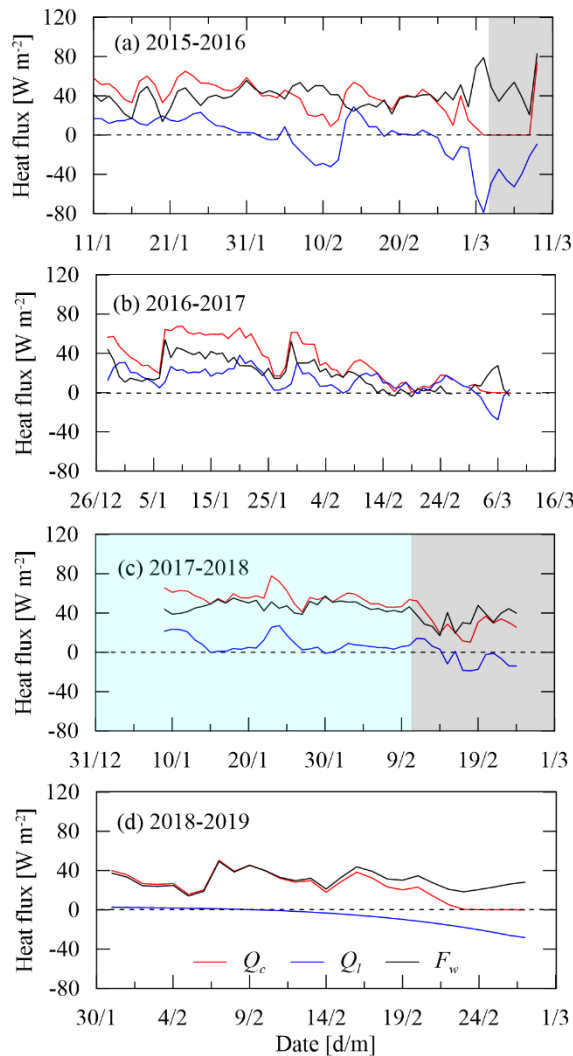
296 Heat and mass fluxes at the ice-water interface govern the basal freezing/melting rate of ice cover and  
 297 the temperature of the top water layer. Our data show that in mid-winter, ice growth slowed down, and  
 298 then a near-equilibrium period appeared (i.e., the thickness kept roughly constant) prior to the start of  
 299 the melting period (Fig. 4). At the ice bottom, the latent heat flux  $Q_l$  kept positive during continuous ice  
 300 growth and fluctuated near zero level during the near-equilibrium period. Thereafter the ice began to  
 301 melt from bottom, and  $Q_l$  turned negative (Fig. 7). The conductive heat flux  $Q_c$  through the bottom ice  
 302 layer kept positive, indicating upward heat transport. After the ice had started fast melting,  $Q_c$  went  
 303 down to near zero with the ice cover turned into a (quasi-)isothermal state.

304 The water-to-ice heat flux  $F_w$  showed a similar variation with  $Q_c$ . Physically,  $F_w$  is crucially determined  
 305 by the inverse thermal gradient of the topmost interface layer. Thinner interface layer with the higher  
 306 thermal gradient in winters 2016 (temporal average  $\pm$  standard deviation:  $40.8 \pm 11.7 \text{ W m}^{-2}$ ) and 2018  
 307 ( $44.9 \pm 9.4 \text{ W m}^{-2}$ ) created higher  $F_w$  than those in winters 2017 ( $21.4 \pm 12.3 \text{ W m}^{-2}$ ) and 2019 ( $30.2 \pm 9.0$   
 308  $\text{W m}^{-2}$ ). Interestingly, the convective mixing process increased  $F_w$  by 33% in winter 2016 but decreased  
 309  $F_w$  by 26% in winter 2018 compared with  $F_w$  before the convection occurrence, indicating complicated  
 310 effects of convection.

311 During the ice growth, both latent heat due to freezing ( $Q_l$ ) and conductive heat from water to ice ( $F_w$ )  
 312 need to be taken out by the ice conduction heat ( $Q_c$ ) (Eq. (4)).  $Q_c$  was predominantly determined by the  
 313 ice thickness and surface heat balance (Leppäranta, 2015), so a higher  $F_w$  meant lower  $Q_l$  and growth  
 314 rate of ice. Specifically,  $F_w$  took up  $> 65\%$  of  $Q_c$  prior to the equilibrium stage (e.g., winters of 2016  
 315 and 2017) and  $> 90\%$  in the equilibrium stage (e.g., winters of 2018 and 2019), the remaining of  $Q_c$   
 316 was used to take the latent heat of freezing out to the atmosphere through the ice cover, leading to  
 317 continuous ice growth.

318 During initial ice melting, the heat transfer from water to ice ( $F_w$ ) was largely conducted through the  
 319 ice cover ( $Q_c$ ) (70%–80%) and partly used to melt the basal ice ( $Q_l$ ). But during the following fast  
 320 melting,  $Q_c$  was negligible since the isothermal ice cover depresses or even prevented heat conduction

321 and  $F_w$  was almost totally used for basal ice melt.



322

323 **Figure 7. Heat fluxes at the ice-water interface ( $Q_c$ : conductive heat flux in the bottom ice;  $Q_i$ :**  
 324 **latent heat flux due to basal ice freezing/melting;  $F_w$ : water-to-ice heat flux). The light gray and**  
 325 **blue zones denote periods of convective mixing and stratification with the local “warm” layer**  
 326 **(Fig. 4), respectively.**

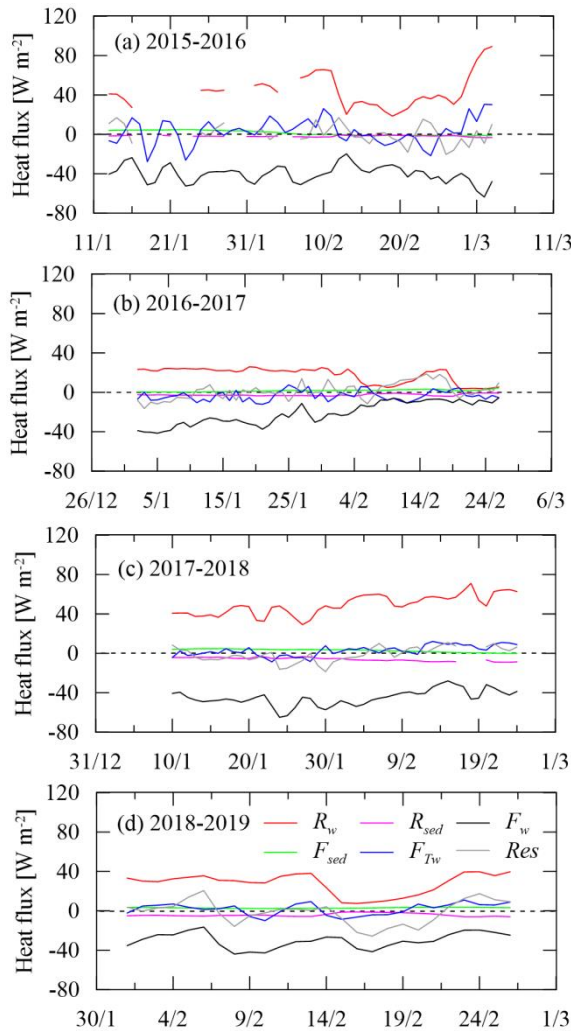
327

### 328 3.4 Energetics of the water column

329 The temperature regime of under-ice water is governed by the heat budget. Fig. 8 shows all the heat  
 330 fluxes involved and the balance residual. In mid-winter, the solar flux  $R_w$  was 25–50  $\text{W m}^{-2}$  under bare  
 331 ice cover and dropped to 1.5–13  $\text{W m}^{-2}$  under ice with a snow cover of varying thickness (1.5–8 cm)  
 332 and age. Only 3%–14% (1–5  $\text{W m}^{-2}$ ) of  $R_w$  (i.e.,  $R_{sed}$ ) reached the sediment surface (Fig. 4), which in  
 333 turn released heat ( $F_{sed}$ ) to the overlying water in mid-winter (1–3  $\text{W m}^{-2}$ ). The heat flux from water to  
 334 ice,  $F_w$ , also showed interannual and seasonal variations (10–60  $\text{W m}^{-2}$ ) and was generally smaller  
 335 under snow-covered ice than that under bare ice, likely indicating the effect of transmitted sunlight.  
 336 The heat content change ( $F_{Tw}$ ) of water, as a resultant heat change from heat sources and sinks, was  
 337 typically small ( $-5$  –  $+4$   $\text{W m}^{-2}$ ) during freezing but grew up to 4–15  $\text{W m}^{-2}$  during the initial melt.  
 338 Evidently, the transmitted solar radiation ( $R_w$ ) and water-to-ice heat transfer ( $F_w$ ) dominated the heat

339 balance of the under-ice water. Combining the 4-winter observations,  $R_w$  was the largest heat source  
 340 ( $34.8 \pm 18 \text{ W m}^{-2}$ ) and accounted for  $(92 \pm 9)\%$  of the total source ( $R_w + F_{sed}$ ) to the under-ice water, while  
 341  $F_w$  was the largest heat sink ( $34.3 \pm 15 \text{ W m}^{-2}$ ) and accounted for  $(96 \pm 38)\%$  of the total sink ( $F_w + R_{sed}$ ).  
 342 The term  $(F_{sed} - R_{sed})$  was only  $-0.8 \pm 2.7 \text{ W m}^{-2}$  and  $F_{Tw}$  was  $0.7 \pm 8.7 \text{ W m}^{-2}$ , both of which can be  
 343 neglected compared to others. Therefore, the transmitted solar radiation was almost totally (97%)  
 344 returned to the ice base by means of water-to-ice heat conduction.

345 Inter-annual comparisons indicated that winter 2017 with only a prevailing inverse temperature  
 346 structure and a decreasing bulk temperature was different from that in other winters (Figs. 4 and 5).  
 347 Heat flows and budget can provide basic insight into the differences. During the freezing period of  
 348 winter 2017, the bulk water temperature kept decreasing because the net heat gain of water was  
 349 negative (i.e.  $R_w + F_{sed} - F_w < 0$ ); Continuous heat loss of water to the ice bottom also created inverse  
 350 thermal gradient and decrease in water temperature prevents the occurrence of mixing. However,  
 351 in other winters (especially 2016 and 2018), the net heat gain of water was positive, so the water  
 352 temperature had an increasing trend, which increases the potential for mixing occurrence.



353  
 354 **Figure 8.** Heat budget of the under-ice water ( $R_w$ : transmitted solar radiation;  $R_{sed}$ : absorbed  
 355 solar radiation by sediment;  $F_w$ : water-to-ice heat flux;  $F_{sed}$ : heat released from sediment;  $F_{Tw}$ :  
 356 sensible heat caused by water heat content change;  $Res$ : residual of heat balancing, which is  
 357 supposed to be zero when all heat fluxes balance ideally)

358

## 359 4 Discussion

### 360 4.1 Comparisons with (sub)Arctic and temperate climate lakes

361 Prior to the ice-on date, in freshwater lakes fall mixing due to thermally free convection (at 3.98°C) and  
362 continuous wind stirring against weak salinity gradients usually create large/full-depth vertical  
363 isothermal structure with temperature quite close to the freezing point (stage I in Fig. 9).

364 After the freeze-up or ice-on, the under-ice stratification evolves as a joint result of snow and ice  
365 condition, solar radiation penetration into water, heat flux from the bottom sediment, and horizontal  
366 advection and diffusion. In Arctic, boreal, and northern temperate regions, such as Fennoscandia, north  
367 America, and central Europe, winter precipitation leads to thick snow cover on lake ice, and only little  
368 sunlight can penetrate through the snow and ice cover and, hence, can be neglected in the water column.  
369 The water column receives heat from the bottom sediment and releases heat to the ice cover on top.  
370 These heat fluxes are small (0–5 W m<sup>-2</sup>), and therefore the lake water stays close to the freezing point  
371 in the top layer and a very weak inverse structure (curve I) through the entire growth period of 3–5  
372 months. After the melting onset, warm air and strengthened solar radiation lead to snow melting, and  
373 more solar radiation goes through the transparent ice and heats up the underlying water, creating a  
374 deepening convective mixing (stage II) before reaching the temperature of maximum density ( $T_m$ )  
375 (stage III). Usually, the ice cover breaks up before the thermal state of stage III forms in most deep  
376 boreal and Arctic lakes (Yang et al., 2020).

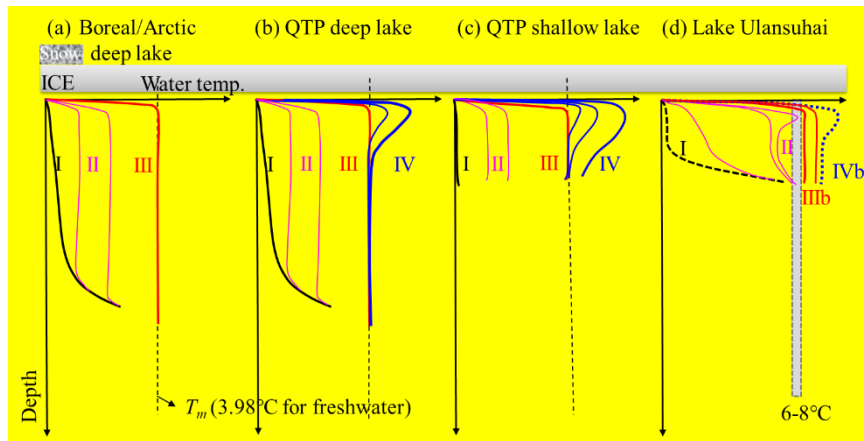
377 In mid-latitude cold and arid regions, intensive solar radiation and thin snow cover allow more solar  
378 energy transmittance to the water column just following the freeze-up. In the Qinghai-Tibet Plateau  
379 (QTP), the water column can keep a stable state of stage I or start slow warming (i.e., period of stage II)  
380 just following the freeze-up in deep lakes, and then go to stage III, creating mid-winter overturn (Fig.  
381 9b). Afterwards, strong solar radiation due to thin ice warms continuously the top water layer (stage  
382 IV), which exists for 4–6 weeks before breakup (Kirillin et al., 2021; Lazhu et al., 2021). However, in  
383 shallow ponds, stage II (i.e., transition from stage I to III) is very short (one week), and the water  
384 column roughly stays at stage III almost over the entire freezing period. The following warm layer (IV)  
385 can deepen to near the lake bottom before ice-off (Fig. 9c) (Huang et al., 2019b).

386 Lake Ulansuhai is very shallow and weakly saline, and although the solar radiation is strong, thermal  
387 stratification dynamics is determined by the synchronous profile evolution of temperature and salinity.  
388 Although our observations covered only the mid-winter, the thermal profile of type I is expected at the  
389 pre-winter and ice-on due to joint effects of wind-stirring and salinity gradient. But stage I should be  
390 very short, and the bulk temperature increases rapidly and transition to stage II takes place due to the  
391 solar radiation transmittance and shallow lake depth. However, the occurrence of convective mixing  
392 (we used stage IIIb here for brackish water) is conditional and mainly dependent upon the salinity  
393 evolution due to the freezing-exclusion effect. Stage IV is also expected since meltwater dilution in the  
394 top layer can suppress the convection. Note that, the forming regime of stage IIIb is different in this  
395 brackish lake compared with stage III in freshwater lakes, which are predominantly driven by  
396 temperature approaching  $T_m$  with solar heating. In brackish lakes, convective mixing may be stopped  
397 by a dicothermal layer in the middle (Fig. 5c) and full convection is possible only when the  
398 bottom water is warm enough to conquer the salt stratification.

399 Salinity structure plays a more important role in lake stratification and convective mixing than the  
400 temperature in brackish/saline and even freshwater lakes with salinity below 0.5 ppt (Kirillin and  
401 Terzhevik, 2011). The present results indicated that the salt exclusion during freezing changes both the



402 total salt content and salinity structure. For instance, for a lake with a mean depth of 1.0 m, if the  
 403 salinity segregation coefficient is assumed 0.15 (Pieters and Lawrence, 2009; Bluteau et al, 2017),  
 404 formation of 0.5 m ice cover can cause an increment of 70% to the water salinity. In Lake Ulansuhai,  
 405 the salinity increases downward at the ice-on with a large salinity gradient. Afterwards, as the ice grows,  
 406 salt exclusion gradually decreases the salinity gradient, making the water more prone to mix  
 407 convectively.



408  
 409 **Figure 9. Typical thermal stratification types in ice-covered lakes: (a) deep lake in Arctic (Jakkila**  
 410 **et al., 2009), (b) deep lakes in QTP (Kirillin et al., 2021; Lazhu et al., 2021), (c) a shallow pond in**  
 411 **QTP (Huang et al., 2019b), and (d) Lake Ulansuhai. The definitions of Roman numbers are**  
 412 **presented in the text.**

#### 413 4.2 What leads to high water-to-ice heat flux?

414 The water-to-ice heat flux  $F_w$  plays a predominant role in the basal growth and melting of lake ice  
 415 cover but is quite challenging to observe instrumentally. Eqs. (1) and (4) provide two ways to estimate  
 416  $F_w$  indirectly if the ice thickness, temperature profile of the ice-water-sediment column, and solar  
 417 irradiance are observed (actually these variables were often observed in lake thermal regime and ice  
 418 programs).

419 By definition,  $F_w$  is the conductive heat flux across the very thin diffusive water layer just beneath the  
 420 ice. The temperature gradient and thickness of this thin layer are influenced to a varied extent by  
 421 thermal stratification, convective mixing (Figs. 5 and 6), advection (Rizk et al., 2014; Kirillin et al.,  
 422 2015), and seiche oscillation (Kirillin et al., 2018). All these thermal and hydraulic processes lead to  
 423 non-stationary and spatiotemporally varying  $F_w$  (Winters et al., 2019).

424 In freshwater lakes, under-ice convective mixing is observed to increase heat transport to the ice  
 425 bottom by increasing the thermal gradient of the interfacial layer above the convective layer (Mironov  
 426 et al., 2002; Kirillin et al., 2018). However, in weakly saline Lake Ulansuhai, under-ice convective  
 427 mixing does not necessarily take place every winter and its impact on heat transport to the ice bottom  
 428 differs annually. In the winter of 2016, the convective mixing developed even across the entire water  
 429 column, and then encroached the overlying interfacial diffusive layer and increased the bottom  
 430 temperature of this layer (Fig 5a), resulting in an increase in the thermal gradient of this layer and thus  
 431 enhancing the heat diffusion (i.e., increasing  $F_w$ ). However, in the winter of 2018, the convection took  
 432 place only in the lower half of the water column, slightly decreased the thermal gradient of the  
 433 overlying diffusive layer, and eliminated the dicothermal layer that maintained relatively high  $F_w$   
 434 prior to the convection onset (Fig 5c), leading to a decrease in  $F_w$ . In the future, the detailed

435 synchronous datasets on synchronous temperature and salinity profiles are needed to understand  
436 the accurate regime of convection in this type of lakes.

437 Although we did not acquire concurrent salinity profiles to the water temperature, sampling results in  
438 the winter of 2017 inevitably indicate the development of double diffusion as the temperature  
439 destabilizes while the salinity stabilizes the stratification (Schmitt, 1994; Schmid et al., 2010). The  
440 effective heat diffusivity of the bulk water column estimated from  $F_w$  derived by Eq. (4) was 5–16  
441 (mean of approximately 10) times larger than the molecular diffusivity, indicating the significantly  
442 enhanced diffusivity of heat due to the double diffusion.

443 In boreal and Arctic lakes, weak solar radiation, short insolation duration, and most importantly thick  
444 snow cover limit solar heat input to the under-ice water column, just water and sediment heat release  
445 (both very small) can cause only low seasonal values,  $F_w < 15 \text{ W m}^{-2}$  (Malm et al., 1997; Jakkila et al.,  
446 2009). However, in arid or mid-latitude lakes with thin snow and/or more intensive solar insolation,  $F_w$   
447 can be high, 10–50  $\text{W m}^{-2}$  in Lake Baikal (Aslamov et al., 2017) and 20–100  $\text{W m}^{-2}$  in QTP lakes with  
448 distinct seasonal variation (Huang et al., 2019a,b; Kirillin et al., 2021). The estimated  $F_w$  in Lake  
449 Ulansuhai is comparable to Lake Baikal and QTP lakes, indicative of the vital contribution of solar  
450 radiation and the absence of snow cover.

451 Higher  $F_w$  does not necessarily mean growth suspend, shorter freezing duration, or thinner lake ice  
452 cover. In Lake Ulansuhai, in ice growth, the conductive heat in the ice cover ( $Q_c$ ) is much higher, which  
453 means that the  $F_w$  can be totally released through the ice cover and the freezing latent heat ( $Q_l$ ) can also  
454 be taken out since  $F_w + Q_l = Q_c$ . This ensures the continuous growth of ice. In ice melting, the  $Q_c$  is  
455 usually ignorable, the under-ice water supplies heat ( $F_w$ ) to maintain basal ice melting ( $Q_l$ ). Higher  $F_w$   
456 means a greater melting rate.

457 From a perspective of heat balance in water (Eq. 1),

$$458 F_w = R_w - R_{sed} + F_{sed} + F_h - \rho_w c_w h_w \frac{dT_w}{dt} - \rho_w c_w T_w \frac{dh_w}{dt}, \quad (5)$$

459 If we define  $Q_{rad} = R_w - R_{sed}$  (i.e., solar absorption by the water column), and the heat content  
460 change due to subsurface water seepage is negligible, Eq. (5) is transformed to

$$461 F_w = Q_{rad} + F_{sed} + F_h - F_{T_w}, \quad (6)$$

462 which means the solar energy ( $Q_{rad}$ ) and sediment heat ( $F_{sed}$ ) are used to change the bulk water  
463 temperature ( $F_{T_w}$ ) and its structure. In turn, the water body loses heat to the ice by adjusting its bulk  
464 temperature and structure.  $R_{sed}$  is usually very small, so,

$$465 Q_{rad} \approx R_w. \quad (7)$$

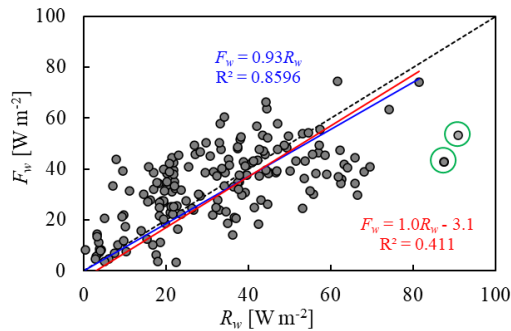
466 And Eq. (6) can be transformed to a simple linear formula to present the contribution of  $R_w$ ,

$$467 F_w = aR_w + b, \quad (8)$$

468 where slope  $a$  reflects the contribution of the penetrated solar radiation while intercept  $b$  reflects the  
469 integrated contributions of other heats. Fig. 8 argued that both  $F_{sed}$  and  $F_{T_w}$  are very small and roughly  
470 constant and  $R_w$  and  $F_w$  are the overwhelming dominant heat source and sink, respectively. In  
471 consequence, if we fit the  $F_w \sim R_w$  data using  $a=1$ , the regressed mean contribution of heat fluxes except  
472 is  $-3.1 \text{ W m}^{-2}$  (red line in Fig. 10), very close to the estimate of  $-1.5 \text{ W m}^{-2}$  in Section 3.4. If we ignore  
473 the minor intercept, the line with  $a=0.93$  explains approximately the same amount of variance in the  
474 observations (blue line in Fig. 10), consistent with the observed ratio of  $F_w$  to  $R_w$  (0.97).

475 But we have to note that values of both coefficients should be lake specific. Lake depth and salinity  
476 modify the changes in convective mixing depth, bulk water temperature, and temperature structure  
477 caused by solar irradiance (Lazhu et al., 2021), and thus alter the relative contributions of solar

478 radiation to water heat content and to heat transfer from water to ice. For instance, in a deep Lake with  
479 a mean depth of 20 m in Finland, 1/3 of the transmitted solar radiation returned to ice (Leppäranta et al.,  
480 2019).



481  
482 **Figure 10. Linear fitting of daily water-to-ice heat flux  $F_w$  as a function of penetrated solar**  
483 **radiation  $R_w$ , the black dashed line denotes  $F_w = R_w$ . Two models were used to fit the data with**  
484 **two dots in green circles being removed.**

## 485 5 Conclusions

486 We present the ice-covered lake thermodynamics in a mid-latitude, cold and dry region, where the  
487 climatic and hydrological environment is in distinct contrast to the Arctic, boreal, and other northern  
488 temperate regions. The ice cover is always bare or covered by only occasional thin snow patches  
489 lasting for 1–2 weeks due to the arid climate and wind blowing. The clear congelation ice cover allows  
490 1/5–1/3 of incident solar radiation to penetrate into the water column in mid-winter, providing a  
491 background for the energetics of under-ice water. The transmitted radiation and heat transfer across the  
492 ice-water interface dominate the heat budget of the water column and are highly correlated. High  
493 water-to-ice heat flux  $F_w$  (daily averages of 20–45  $\text{W m}^{-2}$ ) was observed compared to that in  
494 (sub)Arctic and boreal lakes and takes up >90% of the solar radiation input to the under-ice water (20–  
495 50  $\text{W m}^{-2}$ ). Snow accumulations can decrease  $F_w$  due to its large albedo and light attenuation. Despite  
496 of high  $F_w$ , higher heat conduction within the ice cover (30–55  $\text{W m}^{-2}$ ) existed during the freezing  
497 period because of the persistent snow-free ice surface and created continuous basal growth of ice. In  
498 particular, the high correlation between  $F_w$  and penetrating solar radiation indicates the temporal  
499 variation of  $F_w$ , which is important for updating  $F_w$  parameterization in lake ice modelling.

500 Both bulk water temperature and its structure show diurnal, synoptical, and seasonal variations due to  
501 their quick responses to transmitted radiation and snow events because of the small lake depth. Double  
502 diffusion should surely prevail in wintertime in this shallow saline lake and strengthens the heat  
503 transport to the ice bottom because there is always cooler and fresher water overlying warmer and  
504 saltier water. Under-ice convective mixing and/or dicothermal water layer take place in some winters  
505 depending on the dynamic interaction between radiation (temperature) and salinity stratifications,  
506 which is mediated by the salt exclusion during freezing. However, details in double diffusion,  
507 convective mixing, and the effect of salt exclusion (or cryoconcentration) on water stratification in  
508 shallow ice-covered saline lakes need to be investigated in the future using high-frequency and  
509 high-resolution measurements.

510

511 *Data availability.* The main datasets on lake ice/snow thickness, temperatures, and transmitted solar  
512 radiation used in this paper are available at <https://zenodo.org/record/4291840> (doi:  
513 10.5281/zenodo.4291840).

514

515 *Author contributions.* WH, ML, and ZLi conceived the study. WZ, HY, and ZLin conducted the field  
516 observations. WZ, CZ, RL, and ZLi analysed data on meteorology and ice/snow conditions. WH and  
517 ML developed and ran the model. WZ, RL, and WH calculated the heat budgets for the water column.  
518 WH and WZ wrote the paper with contributions from all the co-authors.

519

520 *Competing interests.* The authors declare no competing interests.

521

522 *Acknowledgements.* This study was funded by the National Key Research and Development Program of  
523 China (2019YFE0197600), National Natural Science Foundation of China (51979024), the Open Fund  
524 of State Key Laboratory of Frozen Soil Engineering (SKLFSE201813), the Program of Introducing  
525 Talents of Discipline to Universities (B08039), the Fundamental Research Funds for the Central  
526 Universities (CHD) (300102291507), and Academy of Finland (333889). We are grateful to the  
527 technicians of the National Ecologic Station in Lake Ulansuhai and the rest of our field team for their  
528 invaluable help in field campaigns.

529

## 530 **References**

531 Aslamov, I.A., Kozlov, V.V., Kirillin, G.B., Mizandrontsev, I.B., Kucher, K.M., Makarov, M.M., and Granin, N.G.:

532 A study of heat transport at the ice base and structure of the under-ice water layer in southern Baikal, Water  
533 Resour. 44(3), 428–441, 2017.

534 Bernhardt, J., Engelhardt, C., Kirillin, G., and Matschullat, J.: Lake ice phenology in Berlin-Brandenburg from

535 1947–2007: observations and model hindcasts, Climatic Change, 112, 791–817, 2012.

536 Bluteau, C. E., Pieters, R., Lawrence, G. A., The effects of salt exclusion during ice formation on circulation in

537 lakes, Environ. Fluid Mech., 17, 579-590, 2017.

538 Bouffard, D., Zdorovenova, G., Bogdanov, S., Efremova, T., Lavanchy, L., Palshin, N., Terzhevik, A., Vinnå, L.

539 R., Volkov, S., Wüest, A., Zdorovenov, R., and Ulloa, H. N.: Under-ice convection dynamics in a boreal lake,

540 Inland Waters, doi: 10.1080/20442041.2018.1533356, 2019.

541 Cavaliere E., and Baulch, H. M.: Denitrification under lake ice. Biogeochemistry, 137(3), 285-295, 2018.

542 Franz, D., Mammarella, I., Boike, J., Kirillin, G., Vesala, T., Bornemann, N., Larmanou, E., Lang, M., and Sachs,

543 T.: Lake-atmosphere heat flux dynamics of a thermokarst lake in arctic Siberia, J. Geophys. Res.: Atmos., 123,

544 5222–5239. <https://doi.org/10.1029/2017JD027751>, 2018.

545 Griffiths, K., Michelutti, N., Sugar, M., Douglas, M. S. V., and Smol, J. P.: Ice-cover is the principal driver of

546 ecological change in High Arctic lakes and ponds, PLoS ONE, 12(3), e0172989.

547 doi:10.1371/journal.pone.0172989, 2017.

548 Huang, W., Cheng, B., Zhang, J., Zhang, Z., Vihma, T., Li, Z., and Niu, F.: Modeling experiments on seasonal

549 lake ice mass and energy balance in the Qinghai-Tibet Plateau: a case study, Hydrol. Earth Syst. Sci. 23,

550 2173-3186, 2019a.

551 Huang, W., Zhang, J., Leppäranta, M., Li, Z., Cheng, B., and Lin, Z.: Thermal structure and water-ice heat transfer

552 in a shallow ice-covered thermokarst lake in central Qinghai-Tibet Plateau, J. Hydrol., 578, 124122, doi:

553 10.1019/j.jhydrol.2019.124122, 2019b.

554 Huang, W., Zhang, Z., Li, Z., Leppäranta, M., Arvola, A., Song, S., Huotari, J., and Lin, Z.: Under-ice dissolved

555 oxygen and metabolism dynamics in a shallow lake: The critical role of ice and snow, Water Resour. Res., 57,

556 e2020WR027990, doi: 10.1029/2020WR027990, 2021.

557 Jakkila, J., Leppäranta, M., Kawamura, T., Shirasawa, K., Salonen, K.: Radiation transfer and heat budget during

558 the ice season in Lake Pääjärvi, Finland, *Aquat. Ecol.*, 43, 681–692, 2009.

559 Karetnikov, S., Leppäranta, M., and Montonen, A.: A time series of over 100 years of ice seasons on Lake Ladoga,  
560 *J. Great Lakes Res.*, 43, 979–988, 2017.

561 Kirillin, G., Aslamov, I., Leppäranta, M., Lindgren, E.: Turbulent mixing and heat fluxes under lake ice: the role of  
562 seiche oscillations, *Hydrol. Earth Syst. Sci.*, 22, 6493–6504, doi:10.5194/hess-22-6493-2018, 2018..

563 Kirillin, G.B., Forrest, A.L. Graves, K.E., Fischer, A., Engelhardt, C., and Laval, B.E.: Axisymmetric circulation  
564 driven by marginal heating in ice-covered lakes, *Geophys. Res. Lett.*, 42, 2893–2900, 2015.

565 Kirillin, G., Leppäranta, M., Terzhevik, A., Granin, N., Bernhardt, J., Engelhardt, C., Efremova, T., Golosov, S.,  
566 Palshin, N., Sherstyankin, P., Zdorovenнова, G., and Zdorovenнов, R.: Physics of seasonally ice-covered lakes:  
567 a review, *Aquat. Sci.*, 74, 659–682, 2012.

568 Kirillin, G., Shatwell, T., and Wen, L.: Ice-covered lakes of Tibetan plateau as solar heat collectors, *Geophys. Res.*  
569 *Lett.*, 48, e2021GL093429, 2021.

570 Kirillin, G., Terzhevik, A.: Thermal instability in freshwater lakes under ice: Effect of salt gradients or solar  
571 radiation?, *Cold Reg. Sci. Technol.* 65(2), 184-190, 2011.

572 Lazhu, Yang, K., Hou, J., Wang, J., Lei, Y., Zhu, L., Chen, Y., Wang, M., and He, X.: A new finding on the  
573 prevalence of rapid water warming during lake ice melting on the Tibetan Plateau, *Science Bulletin*,  
574 <https://doi.org/10.1016/j.scib.2021.07.022>, 2021.

575 Leppäranta, M.: Freezing of lakes and the evolution of their ice cover, Springer, Berlin, Heidelberg, 2015.

576 Leppäranta, M., Lindgren, E., Wen, L., and Kirillin, G.: Ice cover decay and heat balance in Lake Kilpisjärvi in  
577 Arctic tundra, *J. Limnol.*, 78, doi:10.4081/jlimnol.2019.1879, 2019.

578 Lei, R., Leppäranta, M., Cheng, B., Heil, P., and Li, Z.: Changes in ice-season characteristics of a European Arctic  
579 lake from 1964 to 2008, *Climatic Change*, 115(3-4), 725-739, 2012.

580 Lu, P., Cao, X., Li, G., Huang, W., Leppäranta, M., Arvola, L., Huotari, J., and Li, Z.: Mass and heat balance of a  
581 lake ice cover in the central Asian arid climate zone, *Water*, 12, 2888, doi:10.3390/w12102888, 2020.

582 Malm, J., Terzhevik, A., Bengtsson, L., Bovarinov, P., Glinsky, A., Palshin, N., and Petrov, M.: Temperature and  
583 salt content regimes in three shallow ice-covered lakes 2. Heat and mass fluxes, *Hydrol. Res.*, 28, 129–152,  
584 1997.

585 Mironov, D., Terzhevik, A., Kirillin, G., Jonas, T., Malm, J., Farmer, D.: Radiatively-driven convection in  
586 ice-covered lakes: Observations, scaling and mixed-layer model, *J. Geophys. Res.*, 107(C4), 3032, doi:  
587 [10.1029/2001JC000892](https://doi.org/10.1029/2001JC000892), 2002.

588 Pieters, R., Lawrence, G. A.: Effect of salt exclusion from lake ice on seasonal circulation, *Limnol. Oceanogr.*,  
589 54(2), 401-412, 2009.

590 Ptak, M., Sojka, M., and Nowak, B.: Effect of climate warming on a change in the thermal and ice conditions in  
591 the largest lake in Poland-Lake Śniardwy, *J. Hydrol. Hydromech.*, 68(3), 260-270, 2020.

592 Rizk, W., Kirillin, G., and Leppäranta, M.: Basin-scale circulation and heat fluxes in ice-covered lakes, *Limnol.*  
593 *Oceanol.*, 59(2), 445–464, 2014.

594 Shi, L., Li, Z., Niu, F., Huang, W., Lu, P., Feng, E., Han, H.: Thermal diffusivity of thermokarst lake ice in Beiluhe  
595 basin of the Qinghai-Tibet Plateau, *Ann. Glaciol.*, 55(66), 153-158, 2014.

596 Schmid, M., Busbridge, M., Wüest, A.: Double-diffusive convection in Lake Kivu, *Limnol. Oceanogr.*, 55(1),  
597 225-238, 2010.

598 Schmitt, R. W.: Double diffusion in oceanography, *Ann. Rev. Fluid Mech.*, 26(1), 255–285, 1994.

599 Song, S., Li, C., Shi, X., Zhao, S., Tian, W., Li, Z., Bai, Y., Cao, X., Wang, Q., Huotari, J., Tulonen, T., Uusheimo,  
600 S., Leppäranta, M., Loehr, J., and Arvola, L.: Under-ice metabolism in a shallow lake in a cold and arid climate,  
601 *Freshwater Biol.*, <http://doi.org/10.1111/fwb.13363>, 2019.

602 Sun, B., Li, C. Y., Cordovil, C. M. D. S., Jia, K. L., Zhang, S., de Varennes, A., and Pereira, L. S.: Variability of  
603 water quality in Ulansuhai Lake receiving drainage water from Hetao Irrigation system in Yellow River Basin,  
604 China, *Fresen. Environ. Bull.*, 22(6), 1666-1676, 2013.

605 Sun, B., Li, C. Y., and Zhu, D. N.: Changes of Ulansuhai Lake in past 150 years based on 3S technology,  
606 International Conference on Remote Sensing IEEE, doi:10.1109/rsete.2011.5964944, 2011.

607 Verpoorter, C., Kutser, T., Seekell, D. A., and Tranvik, L. J.: A global inventory of lakes based on high-resolution  
608 satellite imagery, *Geophys. Res. Lett.*, 41(18), 6396-6402, 2014.

609 Volkov, S., Bogdanov, S., Zdorovenov, R., Zdorovenova, G., Terzhevik, A., Palshin, N., Bouffard, D., and  
610 Kirillin, G.: *Environ. Fluid Mech.*, 19, 751-764, 2019.

611 Wang, B., Ma, Y., Chen, X., Ma, W., Su, Z., and Menti, M.: Observation and simulation of lake-air heat and  
612 water transfer processes in a high-altitude shallow lake on the Tibetan Plateau, *J. Geophys. Res. Atmos.*, 120, 12  
613 327–12 344, 2015.

614 Winters, K. B., Ulloa, H. N., Wüest, A., and Bouffard, D.: Energetics of radiatively heated ice-covered lakes,  
615 *Geophys. Res. Lett.*, 45, 8913-8925, 2019.

616 Yang, B., Wells, M. G., McMeans, B. Dugan, H. A., Rusak, J. A., Weyhenmeyer, G. A., Brentrup, J. A., Hrycik, A.  
617 R., Laas, A., Pilla, R. M., Austin, J. A., Blanchfield, P. J., Carey, C. C., Guzzo, M. M., Lottig, N. R., Mackay,  
618 M. D., Middel, T. A., Pierson, D. C., Wang, J., and Young, J. D.: A new thermal categorization of ice-covered  
619 lakes, *Geophysical Research Letters*, doi: 10.1029/2020GL091374, 2020.

620 Yang, F., Cen, R., Feng, W., Zhu, Q., Leppäranta, M., Yang, Y., Wang, X., Liao, H.: Dynamic simulation of nutrient  
621 distribution in lakes during ice cover growth and ablation, *Chemosphere*, 281, 130781,  
622 <https://doi.org/10.1016/j.chemosphere.2021.130781>, 2021.

623 Yang, F., Li, C., Leppäranta, M., Shi, X., Zhao, S., and Zhang, C.: Notable increases in nutrient concentrations in a  
624 shallow lake during seasonal ice growth, *Water Sci. Technol.*, 74(12), 2773-2883, 2016.

625 Zhu, D. N., Cathryn, R. M., Sun, B., and Li, C. Y.: The influence of irrigation and Ulansuhai Lake on groundwater  
626 quality in eastern Hetao Basin, Inner Mongolia, China, *Hydrogeol. J.*, 22 (5), 1101-1114, 2014.